Reconfigurable inverse-designed phase-change photonics

Changming Wu[1], Ziyu Jiao[1], Haoqin Deng[1], Yi-Siou Huang[2,3], Heshan Yu[2,3], Ichiro Takeuchi[3], Carlos A. Ríos Ocampo[2,3] and Mo Li[1,4,*]

[1]Department of Electrical and Computer Engineering, University of Washington, Seattle, WA 98195, USA

[2]Department of Materials Science and Engineering, University of Maryland, College Park, MD 20742, USA

[3]Institute for Research in Electronics and Applied Physics, University of Maryland, College Park, MD 20742, USA

[4]Department of Physics, University of Washington, Seattle, WA 98195, USA

Abstract

Chalcogenide phase-change materials (PCMs) offer a promising approach to programmable photonics thanks to their nonvolatile, reversible phase transitions and high refractive index contrast. However, conventional designs are limited by global phase control over entire PCM thin films between fully amorphous and fully crystalline states, which restricts device functionality and confines design flexibility and programmability. In this work, we present a novel approach that leverages pixel-level control of PCM in inverse-designed photonic devices, enabling highly reconfigurable, multi-functional operations. We integrate low-loss Sb_2Se_3 onto a multi-mode interferometer (MMI) and achieve precise, localized phase manipulation through direct laser writing. This technique allows for flexible programming of the photonic device by adjusting the PCM phase pattern rather than relying on global phase states, thereby enhancing device adaptability. As a proof of concept, we programmed the device as a wavelength-division multiplexer and subsequently reconfigured it into a mode-division multiplexer. Our results underscore the potential of combining inverse design with pixel-wise tuning for next-generation programmable phase-change photonic systems.

---

[*] Corresponding author: moli96@uw.edu

Introduction

There are growing interests in programmable photonic integrated circuits (PICs) to enable highly flexible photonic networks for emerging applications such as optical computing[1,2], communication[3,4], optical interconnects for neural network accelerators[5–7], and quantum computing[8–10]. A critical factor in achieving these programmable PICs is the development of compact, high-performance programmable photonic components. Chalcogenide phase-change materials (PCMs) present a promising solution to realize programmable photonics due to their nonvolatile, reversible microstructural phase transition, ability for multilevel operation, and significant refractive index contrast between crystalline and armorphous phases ($\Delta n > 0.5$) [11–14]. PCMs, including $Ge_2Sb_2Te_5$, GSST, Sb_2Se_3, or Sb_2S_3, have been incorporated in Mach–Zehnder interferometers (MZIs)[15,16] and directional couplers[17,18] for phase modulation and in ring resonators for resonance tuning[19,20]. Typically, the functionality of these devices is determined by the phase state of the entire PCM film, whether in binary or multilevel configurations. In conventional designs, a thin film of PCM is deposited onto a photonic structure, with its phase controlled experimentally via thermal stimuli—either electrically using ocal heaters or optically through global tuning pulses. However, these programming methods offer limited spatial resolution, enabling phase control only over the whole PCM area. This constraint introduces challenges when designing programmable PCM photonic devices, as its programmable functions must correspond to fully amorphous and fully crystalline phases across the entire PCM layer. This constraint of device functionality to the phase condition of the entire PCM thin film restricts both its programmability and the full potential for reconfigurability, which is a missed opportunity given the significant index contrast PCMs offer. On the other hand, subdevice pixel-wise manipulation of PCM using laser writing has been demonstrated, allowing for localized programming[21]. However, the iterative process of switching individual PCM pixels is complex and inefficient, making it unsuitable for scalable implementations. To overcome the limitation, advanced design optimization techniques, including genetic algorithms[22,23], semi-analytical approaches[24,25], and notably, inverse design[26,27], can be applied to enhance the programmability of PCM-integrated photonic devices. Inverse design, in particular, has expanded the exploration of design spaces, allowing for the creation of devices with compact footprints and superior performance metrics[28]. Despite some progress, current implementations of inverse design for PCM

devices primarily rely on patterning PCM materials into fixed patterns[29,30] , while phase tuning is still achieved by switching the entire PCM region. The potential for subdevice pixel-wise control in inverse-designed PCM devices has yet to be fully leveraged, leaving substantial room for future advancements.

In this study, we present a reprogrammable, multi-functional photonic device by integrating the low-loss phase-change material Sb_2Se_3 onto a multi-mode interferometer (MMI). Unlike previously reported PCM devices, the function of our MMI is fully encoded by the inverse-designed phase pattern of the PCM. By employing direct laser writing in conjunction with inverse design optimization, we achieve pixel-level resolution in transferring the inverse-designed phase pattern to the Sb_2Se_3 thin film while preserving the integrity of other components. Remarkably, the functionality of this phase-change MMI device is fully rewritable, allowing for the erasure and reconfiguration of the function of the photonic device by reimprinting new phase patterns. As a demonstration, we successfully programmed the device to function as a wavelength-division multiplexing (WDM) device and subsequently reconfigured it into a mode-division multiplexing (MDM) device. Our results showcase the combined potential of inverse design and pixel-wise programming in phase-change photonic devices, paving the way for enhanced functionality and adaptability across different application scenarios.

Results

Figure 1a illustrates the schematic of the proposed reconfigurable multi-functional 1×2 MMI. Each MMI, occupying a footprint of 40×8.5 μm^2, is fabricated on a 330 nm-thick Si_3N_4-on-insulator substrate. A 30 nm-thick low-loss phase-change material, Sb_2Se_3, is sputtered onto the MMI and protected by a 200 nm-thick SiO_2 capping layer. The significant refractive index contrast between the two phases of Sb_2Se_3 (amorphous: $n_a = 3.285$ and crystalline: $n_c = 4.050$, respectively) allows efficient evanescent coupling of light within the MMI with the Sb_2Se_3 thin film. As a result, the light undergoes a phase modulation that depends on the local structure of Sb_2Se_3. By inducing localized perturbations, the phase pattern of Sb_2Se_3 on MMI shapes the wavefront during light propagation, altering the amplitude and phase distribution of the propagating light. This capability allows the MMI to execute diverse functions with minimum loss penalty. In particular, we can associate the specific function of the MMI device with a distinct binary Sb_2Se_3 phase pattern within

the "inverse-design region" highlighted by the red dashed box in Figure 1b. Furthermore, as depicted in Figure 1c, the MMI's function is entirely encoded within the PCM thin film, while the other components remain unchanged. The reversible phase change of Sb_2Se_3 allows for convenient erasure and recreation of the phase pattern, thereby lifting the limitation of binding device functionality to the phase condition of the entire PCM thin film. This enables a more flexible approach to designing the functionality of PCM photonic devices.

Programming the MMIs involves designing and patterning processes. First, we determine the MMI's function and design the corresponding Sb_2Se_3 phase pattern. To achieve this, we employ a topology optimization approach to inverse-design the phase pattern of the Sb_2Se_3 thin film [31,32]. In our simulations, we segment the Sb_2Se_3 thin film within the "inverse-design region" into an array of pixels, each measuring 100 nm × 100 nm × 30 nm, while maintaining the other components of the MMI unchanged during optimization. To avoid unachievably fine features, we also limit the minimum feature size in the designed patterns to be larger than 500 nm. The optimization process initiates with a linear parametrization, allowing the dielectric permittivity ε_i of each pixel to continuously vary in the range of (n_a, n_c). Subsequently, the phase pattern is updated using the steepest descent method. Through this gradual optimization process, the permittivity of the pixels transitioned from an intermediate value in (n_a, n_c) toward a binary value of n_a or n_c. Consequently, the phase map evolved from a grayscale phase pattern to the binary phase pattern of Sb_2Se_3, as illustrated in Figure 2a.

Second, the corresponding phase pattern is directly laser written onto the MMIs using a commercial 405 nm laser direct lithography system (Heidelberg DWL 66+, 405 nm laser). The exceptional speed and accuracy of the DWL system enable efficient and effective patterning of the target MMI device. During the experiment, we began with the Sb_2Se_3 thin film in the completely cSb_2Se_3 phase and wrote phase patterns directly onto the MMI by quenching cSb_2Se_3 into aSb_2Se_3 phase using optical heating[33,34]. Figure 2b displays a series of rectangular aSb_2Se_3 patterns with widths ranging from 200 nm to 2 μm written on a blank cSb_2Se_3 film, demonstrating a minimum feature size of ~300 nm achieved through laser writing. We note that this resolution reaches the subwavelength regime and is much smaller than the resolution achieved in previous works[33,35,36].

Furthermore, the pattern can be readily erased through an annealing process, either by local heating using a continuous-wave laser or global heating to 180 °C using a hotplate (see Figure 2c). By selectively erasing and rewriting the patterns on MMIs, the function of the circuit is reprogrammed. This technique gives us a toolkit for writing high-finesse functional patterns into the phase-change films and modifying or erasing them as required.

Using the direct writing technique, we first demonstrate programming the MMI as a mode demultiplexer (MDM). The Sb_2Se_3 phase pattern (Figure 2e), generated with the inverse design approach, was precisely aligned (misalignment < 125 nm) and written onto the MMI. As shown in Figure 2d, the laser-written phase pattern closely resembles the design with minimal error. Subsequently, we characterized the MDM performance of the MMI device. Figure 3a shows an optical microscope image of the complete photonic circuit and a sketch of the measurement setup. A multimode waveguide, supporting both TE_0 and TE_1 modes, is connected to the input of the MMI, while both output ports (port 2 and port 3) are linked to single-mode waveguides for measurement. The incident light is coupled to the device via either port 1 or port 4 and passes through a mode combiner constructed with an asymmetric directional coupler. This combiner selectively convertthe incoming TE_0 mode from incident port 4 to the TE_1 mode while maintaining the TE_0 mode from input port 1. The design and characterization of the mdoe combiner is included in Supplementary Information. As a result, the input mode to the MMI is determined based on which port is used (port 1 for TE_0 or port 4 for TE_1), which is selected using a 1×2 optical switch. Finally, the output power from both output ports (port 2 and port 3) was measured to determine the respective transmission coefficients of each mode.

Figures 3b and 3c illustrate the MDM's functionality, routing the TE_0 mode to port 2 and the TE_1 mode to port 3 over a wavelength range of 1500 to 1600 nm. Figures 3d and 3e compare the simulated and measured transmission spectra of the two modes. In the simulation, this MDM device demonstrates a modal extinction ratio surpassing 15 dB for both mode channels over a bandwidth wider than 100 nm. The experimental results exhibit a extinction ratio of > 10 dB for both mode channels, lower than the simulated values. We attribute the underperformance to fabrication imperfections, misalignment, and roughness in the phase pattern. Additionally, in our measurements, the grating couplers constrain the insertion loss and operational bandwidth. Furthermore, we fabricated three identically devices, which demonstrated similiar performance

(see Supplementary Information), manifesting the consistency of the design and fabrication approach.

We then demonstrate how this technique enables a more flexible approach to designing the functionality of PCM photonic devices, moving beyond the constraint of binding device functionality to the phase condition of the entire PCM thin film. We reprogram the functionality of the MMI from an MDM to a wavelength demultiplexer (WDM). To do so, we erased the previous Sb_2Se_3 phase pattern and rewrote a newly designed phase pattern onto the same MMI, as shown in Figures 4a to 4c. To accomplish the WDM function, we redesigned the phase pattern within the "inverse-design region" using the same method described earlier (Figure 4d). Figures 4e and 4f show the simulated electric field distribution at two operating wavelengths of 1475 nm and 1625 nm, respectively. The WDM separates the TE_0 mode of the input waveguide into the two output ports according to their wavelength: 1475 nm at port 2 and 1625 nm at port 3. Figures 4g and 4h plot the measured and simulated transmission spectra for the WDM, respectively. The simulation shows a high extinction ratio of > 15 dB at the center wavelengths. The experimental results show a lower extinction ratio of >6 dB measured at wavelengths of 1465 nm and 1695 nm, which is limited by the range of the tunable laser source used. The reduced performance can again be attributed to fabrication imperfections and pattern misalignment. Nevertheless, the results successfully demonstrate a complete change of the device's functionality, from an MDM to a WDM, by recreating the phase pattern of the Sb_2Se_3 thin film.

Conclusion

In summary, our work demonstrates the versatility of a multi-functional photonic device achieved through the integration of low-loss phase-change material Sb_2Se_3 onto a silicon nitride photonic integrated circuit, where functionality is encoded in the phase pattern of the Sb_2Se_3 thin film unlike previous design logic for phase-change photonics that binding device functionality to the phase condition of the entire PCM thin film. Leveraging direct laser writing and inverse design optimization, this novel phase-change MMI device offers excellent flexibility for a single photonic device. We successfully programmed this device to operate as multiplexers for either wavelengths or spatial modes. Utilizing photonic inverse design ensured high extinction ratios and broadband response in both configurations. Moreover, there is potential for further exploration of the

application scenario by adopting a multi-level grayscale design instead of the current binary design and cascading multiple stages of such photonic structures to enable a diverse range of complex reconfigurable photonic systems.

Data Availability Statements
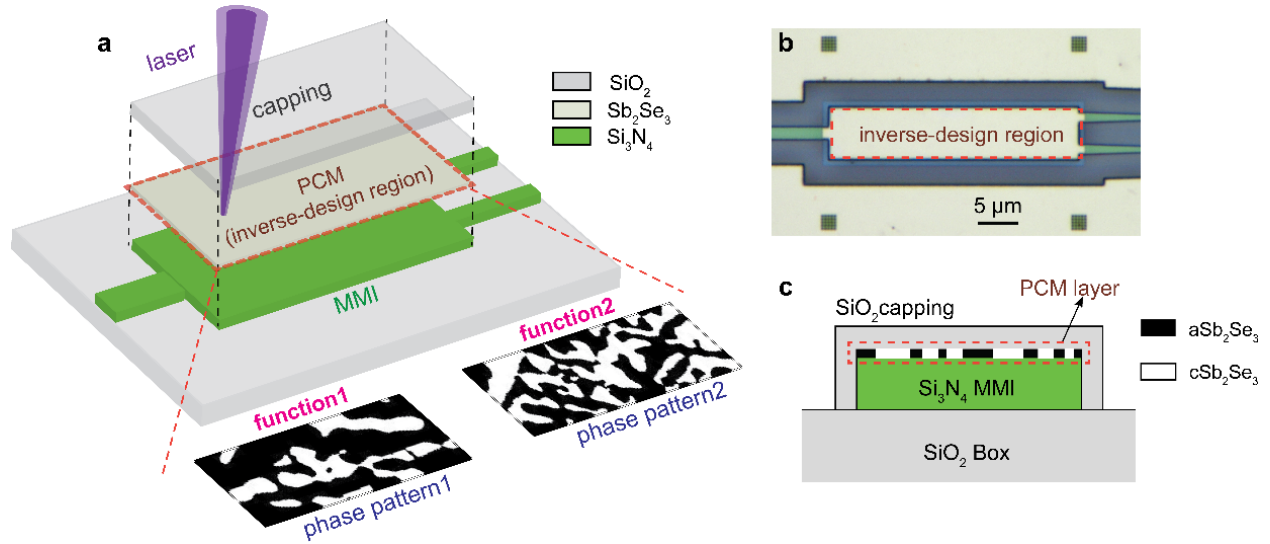
Figure 1 Schematic of the laser writing of multi-functional photonic MMI. a. Illustration of programming a Sb₂Se₃ thin film integrated MMI using a focused laser beam. The commercial direct laser writing system (Heidelberg DWL66+) is used to write/erase various phase patterns onto the Sb₂Se₃ thin film, which determines the function of the MMI. **b.** The top-view optical image of an as-fabricated 40×8 μm^2 MMI. The device's functionality is defined by the Sb₂Se₃ phase pattern in the "inverse design region" (red dashed box). **c.** The cross-sectional schematic of the MMI device with patterned Sb₂Se₃. To change the function of the device, the phase pattern in the Sb₂Se₃ thin film is recreated, while all the other components remain unchanged.
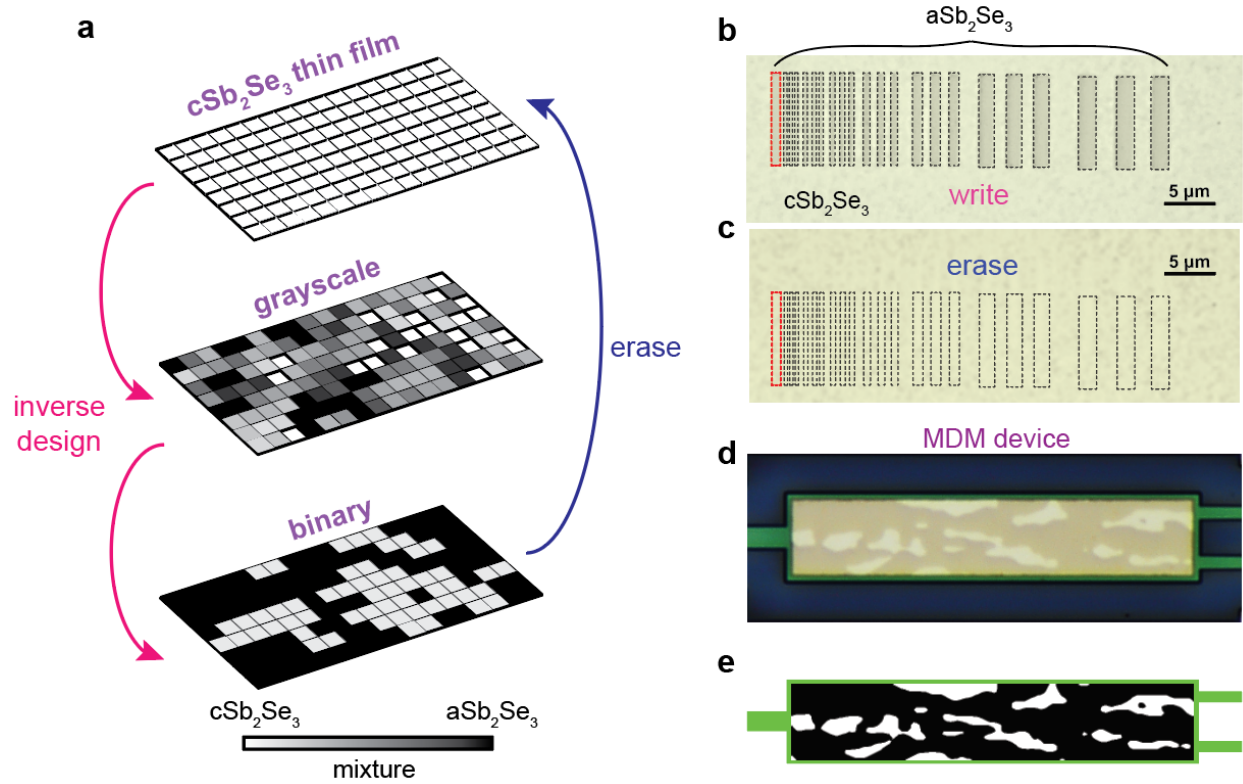
Figure 2 Inverse design of the Sb₂Se₃ phase pattern. **a.** Schematic of the inverse design approach to generate phase pattern for the Sb₂Se₃ MMI. The optimization is initiated with a fully crystalline Sb₂Se₃ thin film, and then the amorphous-crystalline spatial distribution is inverse-designed using the topology optimization method, resulting in a binary phase pattern. White and black areas indicate the crystalline and amorphous Sb₂Se₃, respectively. **b.** Optical image of aSb₂Se₃ rectangular array written on cSb₂Se₃ thin film for testing the writing resolution. The minimum feature size achieved is 300 nm. **c**. The test pattern in (**b**) is erased back to the cSb₂Se₃ phase by thermal annealing. The area marked by dashed lines indicates the initial patterns. **d.** Optical images of an inverse-designed pattern for the mode demultiplexer written in Sb₂Se₃. **e.** The corresponding inverse designed, binarized Sb₂Se₃ phase pattern for the mode demultiplexer.
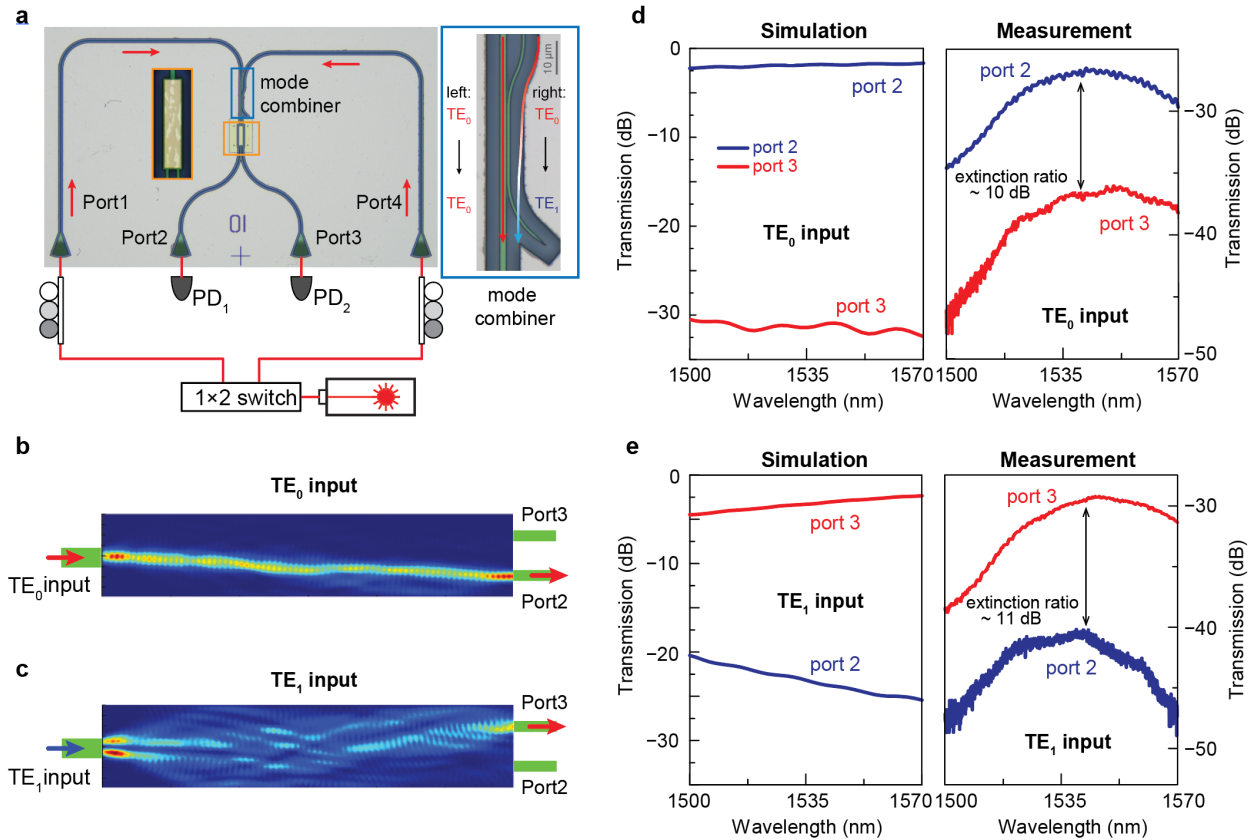
Figure 3. MMI programmed as a mode demultiplexer. a. The optical setup for the MDM device measurement. An optical switch and a mode combiner control the input mode, TE_0 or TE_1, to the MDM. Inset: the optical image of the mode combiner. **b.** and **c.** The simulated $|E|^2$ distribution in the MDM with TE_0 mode input (**c**) and TE_1 mode input (**c**) at the wavelength of 1550 nm. **d** and **e**. The simulated (left column) and measured (right column) transmission spectrum of the mode demultiplexer when the TE_0 mode (**d**) or TE_1 mode (**e**) is input. The lower extinction ratio is attributed to fabrication imperfections and laser writing misalignment.
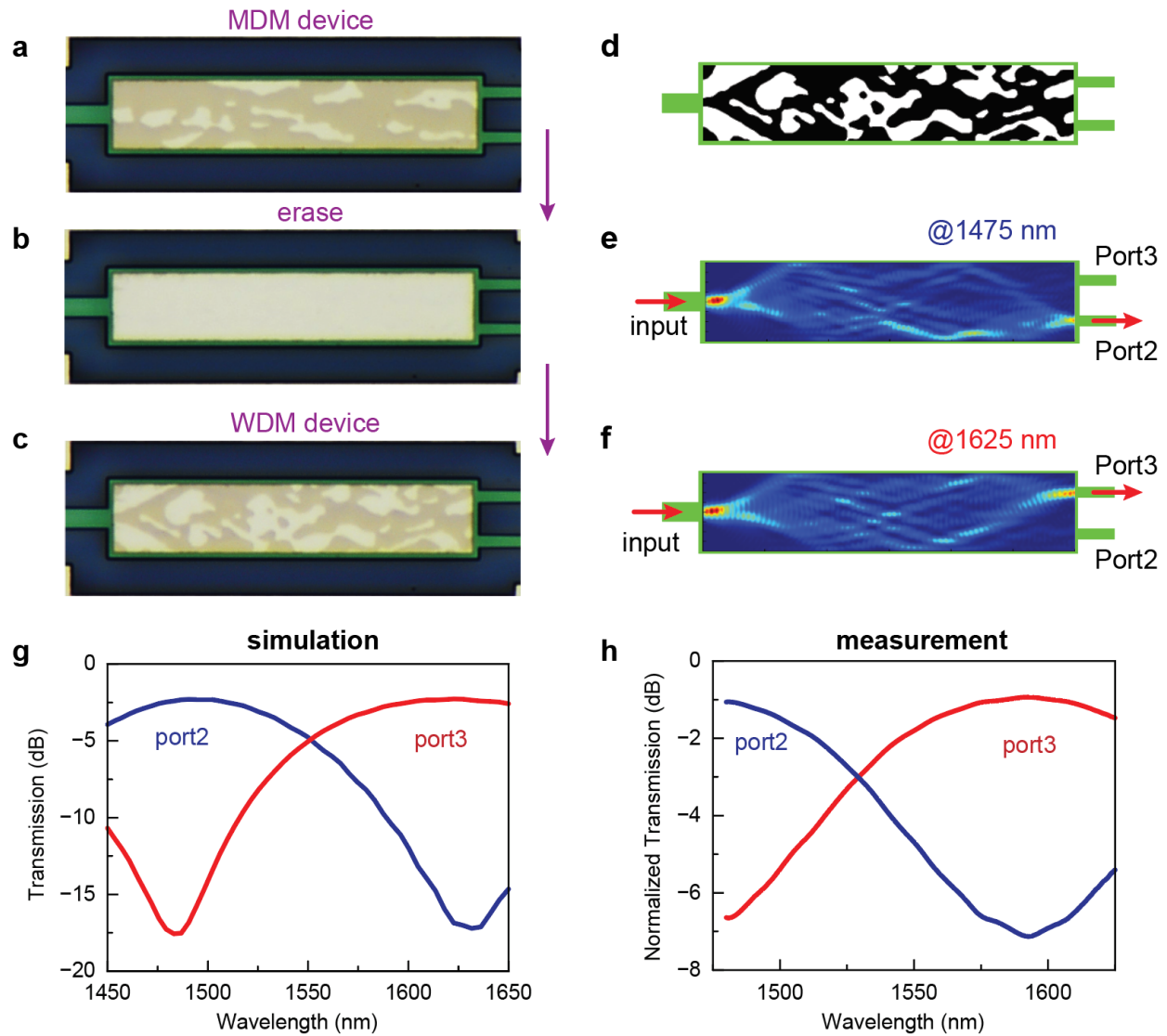
Figure 4 Reprogramming to a wavelength demultiplexer. a to c. Optical images showing the steps that the MDM device (**a**) is first erased to the full crystalline cSb_2Se_3 thin film(**b**) and then reprogrammed as a WDM (**c**). **d.** Inverse-design binarized Sb_2Se_3 phase pattern for the WDM. White and black areas indicate the crystalline and amorphous Sb_2Se_3, respectively. **e** and **f.** Simulated $|E|^2$ distribution of the WDM device operating at 1475 nm (**e**) and 1625 nm (**f**). **g and h.** Transmission spectra to output ports 2 and 3 obtained from simulation (**g**) and measurement (**h**).

Reference

1. Zhou, T. *et al.* Large-scale neuromorphic optoelectronic computing with a reconfigurable diffractive processing unit. *Nat Photonics* **15**, 367–373 (2021).

2. Shastri, B. J. *et al.* Photonics for artificial intelligence and neuromorphic computing. *Nat Photonics* **15**, 102–114 (2021).

3. Yang, K. Y. *et al.* Multi-dimensional data transmission using inverse-designed silicon photonics and microcombs. *Nat Commun* **13**, 7862 (2022).

4. Xu, X. *et al.* Self-calibrating programmable photonic integrated circuits. *Nat Photonics* **16**, 595–602 (2022).

5. Boybat, I. *et al.* Neuromorphic computing with multi-memristive synapses. *Nat Commun* **9**, 2514 (2018).

6. Feldmann, J., Youngblood, N., Wright, C. D., Bhaskaran, H. & Pernice, W. H. P. All-optical spiking neurosynaptic networks with self-learning capabilities. *Nature* **569**, 208–214 (2019).

7. Shastri, B. J. *et al.* Photonics for artificial intelligence and neuromorphic computing. *Nat Photonics* **15**, 102–114 (2021).

8. Wang, J. *et al.* Multidimensional quantum entanglement with large-scale integrated optics. *Science (1979)* **360**, 285–291 (2018).

9. Wang, J., Sciarrino, F., Laing, A. & Thompson, M. G. Integrated photonic quantum technologies. *Nat Photonics* **14**, 273–284 (2020).

10. Madsen, L. S. *et al.* Quantum computational advantage with a programmable photonic processor. *Nature* **606**, 75–81 (2022).

11. Rios, C. *et al.* Integrated all-photonic non-volatile multi-level memory. *Nat Photonics* **9**, 725–732 (2015).

12. Zhang, Y. *et al.* Broadband transparent optical phase change materials for high-performance nonvolatile photonics. *Nat Commun* **10**, 4279 (2019).

13. Delaney, M., Zeimpekis, I., Lawson, D., Hewak, D. W. & Muskens, O. L. A New Family of Ultralow Loss Reversible Phase-Change Materials for Photonic Integrated Circuits: Sb2S3 and Sb2Se3. *Adv Funct Mater* **30**, 2002447 (2020).

14. Prabhathan, P. *et al.* Roadmap for phase change materials in photonics and beyond. *iScience* **26**, 107946 (2023).

15. Ríos, C. *et al.* Ultra-compact nonvolatile phase shifter based on electrically reprogrammable transparent phase change materials. *PhotoniX* **3**, 26 (2022).

16. Yang, X. *et al.* Non-Volatile Optical Switch Element Enabled by Low-Loss Phase Change Material. *Adv Funct Mater* 2304601 (2023).

17.   Xu, P., Zheng, J., Doylend, J. K. & Majumdar, A. Low-Loss and Broadband Nonvolatile Phase-Change Directional Coupler Switches. *ACS Photonics* **6**, 553–557 (2019).

18.   Chen, R. *et al.* Broadband Nonvolatile Electrically Controlled Programmable Units in Silicon Photonics. *ACS Photonics* **9**, 2142–2150 (2022).

19.   Stegmaier, M., Ríos, C., Bhaskaran, H., Wright, C. D. & Pernice, W. H. P. Nonvolatile All-Optical 1 × 2 Switch for Chipscale Photonic Networks. *Adv Opt Mater* **5**, 1600346 (2017).

20.   Fang, Z. *et al.* Ultra-low-energy programmable non-volatile silicon photonics based on phase-change materials with graphene heaters. *Nat Nanotechnol* **17**, 842–848 (2022).

21.   Delaney, M. *et al.* Nonvolatile programmable silicon photonics using an ultralow-loss Sb2Se3 phase change material. *Sci Adv* **7**, eabg3500 (2021).

22.   Liu, C., Maier, S. A. & Li, G. Genetic-algorithm-aided meta-atom multiplication for improved absorption and coloration in nanophotonics. *ACS Photonics* **7**, 1716–1722 (2020).

23.   Ren, Y. *et al.* Genetic-algorithm-based deep neural networks for highly efficient photonic device design. *Photonics Res* **9**, B247–B252 (2021).

24.   Felici, M., Atlasov, K. A., Surrente, A. & Kapon, E. Semianalytical approach to the design of photonic crystal cavities. *Phys Rev B* **82**, 115118 (2010).

25.   Valagiannopoulos, C. & Lagoudakis, P. G. Photonic crystals for optimal color conversion in light-emitting diodes: a semi-analytical approach. *JOSA B* **35**, 1105–1112 (2018).

26.   Piggott, A. Y. *et al.* Inverse design and demonstration of a compact and broadband on-chip wavelength demultiplexer. *Nat Photonics* **9**, 374–377 (2015).

27.   Ahn, G. H. *et al.* Photonic inverse design of on-chip microresonators. *ACS Photonics* **9**, 1875–1881 (2022).

28.   Molesky, S. *et al.* Inverse design in nanophotonics. *Nat Photonics* **12**, 659–670 (2018).

29.   Yin, K., Gao, Y., Shi, H. & Zhu, S. Inverse Design and Numerical Investigations of an Ultra-Compact Integrated Optical Switch Based on Phase Change Material. *Nanomaterials* **13**, 1643 (2023).

30.   Wei, M. *et al.* Inverse design of compact nonvolatile reconfigurable silicon photonic devices with phase-change materials. *Nanophotonics* **13**, 2183–2192 (2024).

31.   Jensen, J. S. & Sigmund, O. Topology optimization for nano-photonics. *Laser Photon Rev* **5**, 308–321 (2011).

32.   Christiansen, R. E. & Sigmund, O. Inverse design in photonics by topology optimization: tutorial. *JOSA B* **38**, 496–509 (2021).

33.   Delaney, M. *et al.* Nonvolatile programmable silicon photonics using an ultralow-loss Sb2Se3 phase change material. *Sci Adv* **7**, eabg3500 (2021).

34.   Wu, C. *et al.* Freeform direct-write and rewritable photonic integrated circuits in phase-change thin films. *Sci Adv* **10**, eadk1361 (2024).

35.   Wang, Q. *et al.* Optically reconfigurable metasurfaces and photonic devices based on phase change materials. *Nat Photonics* **10**, 60–65 (2016).

36.   Liu, H. *et al.* Rewritable color nanoprints in antimony trisulfide films. *Sci Adv* **6**, eabb7171 (2020).